Int. J. Electrochem. Sci., 14 **(2019)** 11225 – 11236, doi: 10.20964/2019.12.59

International Journal of ELECTROCHEMICAL SCIENCE
www.electrochemsci.org

Electrocatalytic Polysulfide Traps and their Conversion to long-chain Polysulfides using rGO-Pt composite as electrocatalyst to Improve the Performance of Li-S Battery

ZhiZhong Xie[1], Guanghui Chen[1], Zhien Liu[2,], Xinxin Zhu[1,3], Dan Liu[1], Rong Li[1], Deyu Qu[1,*], Junsheng Li[1]*

[1] Department of Chemistry, School of Chemistry, Chemical Engineering and Life Sciences, Wuhan University of Technology, 122 Luoshi Road, Wuhan, 430070 Hubei, PR China
[2] School of Automotive Engineering,Wuhan University of Technology, 122 Luoshi Road, Wuhan, 430070 Hubei, PR China
[3] State Key Laboratory of Advanced Technology for Material Synthesis and Processing, Wuhan University of Technology, 122 Luoshi Road, Wuhan, 430070 Hubei, PR China
[*]E-mail: lzen21@whut.edu.cn, deyuquwuhan@163.com

Received: 24 June 2019 / *Accepted:* 28 September 2019 / *Published:* 29 October 2019

Serious shuttle effect and sluggish reaction kinetics are the two major barriers that limit the cathode cycling stability in lithium-sulfur batteries. In this study, we deviate from the prevalent approach compositing sulfur with various carbonaceous materials by introducing electrocatalysis concept in lithium-sulfur chemistries. Two-dimensional graphene has been used as model system to support electrocatalyst Pt. Uniform dispersion of Pt nanoparticles on graphene layers not only demonstrate to preferential adsorption of soluble polysulfide species, but also catalyze efficiently transformation to long-chain polysulfides in the subsequent redox process. The result rGO-Pt/S composite shows a 29.5% enhancement in capacity over pristine rGO/S electrode. More impressively, rGO-Pt/S electrode exhibits good cycling stability at a high rate of 2 C corresponding to a tiny capacity fading rate of 0.01% per cycle over 300 discharge/charge cycles. Thus, this work provides a facile strategy for improving the performance of Li−S batteries toward practical application.

Keywords: Pt; bi-functional electrocatalyst; polusulfide; shuttle-effect

1. INTRODUCTION

In recent year, lithium-sulfur (Li-S) batteries capture unprecedented attention and are expected to the most prospective next-generation battery technologies due to their exceptional theoretical capacity, nature abundant, nontoxicity and low cost, as compared to state-of-the-art Li ion batteries (LIBs) based on insertion-type materials.[1-4] However, fast capacity fading, poor Coulombic efficiency, and corrosion of anode of Li-S batteries are stubborn barriers toward its practical

applications.[5, 6] The fundamental reason behind these complex technical difficulties is the so called "shuttle effect", a process occurred in the entire stage of battery charging and discharging. This mechanism includes diffusion and dissolution of long-chain polysulfides into ether-based electrolytes, followed by passivating the lithium anode, leading to the consuming of the active sulfur and poor cycle life.[7, 8] Additionally, electrical insulation of elemental sulfur and short-chain polysulfides, and severe volumetric expansion cause slow reaction kinetics and electrode pulverization, and increase in cell polarization.[9, 10]

Multifarious strategies have been utilized to settle the above-mentioned issues. Most previous investigations are still concentrated on the design of unique carbon-based hosts with adjustable porous morphologies and controllable structures, such as micro/mesoporous carbon,[11, 12] carbon nanotubes,[13, 14] graphene,[15-18] hollow nanostructure carbon,[19, 20] sandwich-type,[21-23] yolk-shell,[24-26] core-shell nanostructure carbon,[27, 28] and so on. Nevertheless, highly polar and ionic polysulfides (PS) is hard to anchor only by physical adsorption of carbon.[29] Furthermore, the intrinsic issues of pore clogging due to deposition of end products of discharge (Li_2S_2 and Li_2S), instead, cause low sulfur utilization and block conductive pathways for charge transport.[30, 31] Therefore, a more targeted approach is to construct strong chemical interaction between the nonpolar carbon framework and the polar PS. To the best of our knowledge, the discharge process of Li-S batteries consists of three stages of solid/liquid, liquid/liquid, and liquid/solid phase change.[32, 33] In fact, the overall redox reaction is primarily driven by the dissolution of polysulfides into the electrolyte, i.e, dissolution and diffusion of polysulfdes occurring in the preliminary stages of battery discharging are effective at promoting the subsequent reaction and increasing initial capacity for most carbon materials in which sulfur is encapsulated inside. It is worth noting that sluggish polysulfides conversion reaction kinetics caused by the insulation of end products of discharge make Li_2S_2 and Li_2S difficult to be rapidly reduced to elemental sulfur before reaching the cut-off voltage, which result in loss of active material and fast capacity fading. Unfortunately, this issue is often overlooked in the literature. Even in the most recent works, researchers have poured growing attention into the migration of PS, but have rarely conducted detailed investigations on the conversion of end products. On the other hand, electrocatalyst such as Pt and Ni with the hydrophilic and polar nature have been widely used to improve the electrochemical hydrogen insertion into porous carbon materials.[34, 35] Moreover, the application of electrocatalytic electrodes to photoelectrochemical solar cells[36, 37] and redox flow cells[38, 39] can effectively enhance the reaction kinetics of aqueous PS. Consequently, we believe that it is feasible to introduce electrocatalyst Pt into the sulfur cathode to enhance non-aqueous PS redox reactions kinetics.

Herein we deviated from the prevalent approach by exploring electrocatalyst Pt effect on PS redox reactions kinetics. In order to effectively understand catalytic properties of metal Pt, and eliminate the impact of any unique frameworks with well-defined structures on performance improvement, in this work, two-dimensional graphene with high surface area, superior mechanical and electrical properties has been employed to support electrocatalysts.[40] Uniformly dispersed electrocatalyst Pt not only improve the conductivity of electrode, but also tend to form in situ chemisorption with polar natured PS to mitigate the shuttle effect. Further, the existence of electrocatalyst Pt enhances PS conversion reaction kinetics, and is effective at reducing and controlling deposition of end products of discharge (Li_2S_2 and Li_2S). After reduction and followed by injection of sulfur, the resulting rGO-Pt/S electrode with a high

sulfur content (~60 wt%) and areal sulfur loading (~1 mg cm^{-2}) enabled good cycle stability and rate capability.

2. EXPERIMENTAL

2.1. Synthesis

Potassium tetrachloroplatinate (K_2PtCl_4) was obtained from Aladdin reagent Co. The other chemicals were purchased from Sinopharm Chemical Reagent Co., Ltd and used without further purification. Graphite oxide(GO) was prepared from natural graphite powder according to a modified Hummers' method. was prepared from natural graphite powder according to a modified Hummers' method.[41-45] Upon microwave irradiation, a large volume expansion of the GO powders, accompanied by 'boom' was heard. For a typical synthesis, 150 mg reduced graphene oxide (rGO) was dispersed with 150 mL deionized water under ultrasonication to form suspension. Then, 17 mg K_2PtCl_4 was dissolved in 3 mL deionized water and added dropwise to the suspension under vigorous stirring in an ice bath for 1h. After that, 100 mL of water containing excess $NaBH_4$ was added slowly into above solution. The resulting rGO-Pt composite was harvested by collected by suction filtration, washed with deionized water and ethanol and dried at 50 °C. To prepare the carbon/sulfur composite, the sample (rGO-Pt and rGO) and S powder should be uniformly mixed by grinding with a mass ratio of 40:60. The mixture was then sealed in a glass tube in a vacuum and annealed at 400 °C for 5 h.

2.2. Material Characterization

X-ray diffraction (XRD) patterns were carried out on Bruker D8 Advance, Cu Kα radiation. The morphology and structure of all samples were characterized by Scanning electron microscopy (SEM, Hitachi S-4800) with an EDX analysis, and Transmission electron microscopy (TEM, JEM 2100F, 200 kV), respectively. X-ray photoelectron spectroscopy (XPS) data were measured by Thermo VG Multilab 2000.

2.3. Electrochemical Measurements

The electrode was prepared by mixing active materials (80 wt%), Super P (10 wt%), and LA133 (10 wt%) in deionized water. Then, the resultant slurry was cast onto Al foil and dried at 50 °C for 12 h. The 2032 type coin cells were assembled into a half-battery in an argon-filled glove box. Metallic Li anode was used as the counter electrode and Celgard 2400 were adopted as the separator. The electrolyte composed of 1.0 M lithium bis(trifluoromethanesulfonyl)imide (LiTFSI) in a mixture of 1,3-dioxolane (DOL) and 1,2-dimethoxyethane (DME) (1:1 by volume) plus 4.0 wt% $LiNO_3$. Galvanostatic tests were carried out in the potential range of 1.5-2.8 V vs Li/Li^+ at room temperature using a LAND test system at varied current densities The cyclic voltammetry (CV) curves were recorded with a CHI660E electrochemical workstation at a scanning rate of 0.05 mV s^{-1}. Electrochemical impedance spectroscopy

(EIS) was employed in the frequency range from 0.01 Hz to 100 kHz with a perturbation amplitude of 5 mV.

3. RESULTS AND DISCUSSION

Graphene was used in this study as a model system. First, Graphite oxide was prepared by a modified Hummers' method, followed by freeze-drying processes and microwave irradiation treatment. Whereafter, electrocatalyst Pt were successfully dispersed uniformly on such rGO sheets to form on-site chemical adsorption with PS. Sulfur and rGO-Pt were mixed sealed in a glass container in vacuum and thermally treated to yield rGO-Pt/S composite. The pristine rGO without modification was also used as comparison. X-ray diffraction (XRD) pattern of rGO/S and rGO-Pt/S composite are depicted in Figure 1a. Since two-dimensional graphene without any pores to deposit the molten semi-crystalline state sulfur, some characteristic strong sulfur peaks indexed to orthorhombic structure (JCPSD no. 08-0247) could be observed.[46, 47] Nevertheless, layer and ripple-like flake morphology graphene in Figure 1b clearly shows no visible large bulk sulfur particles aggregation, indicating its large special surface area are beneficial for dispersing sulfur particles.

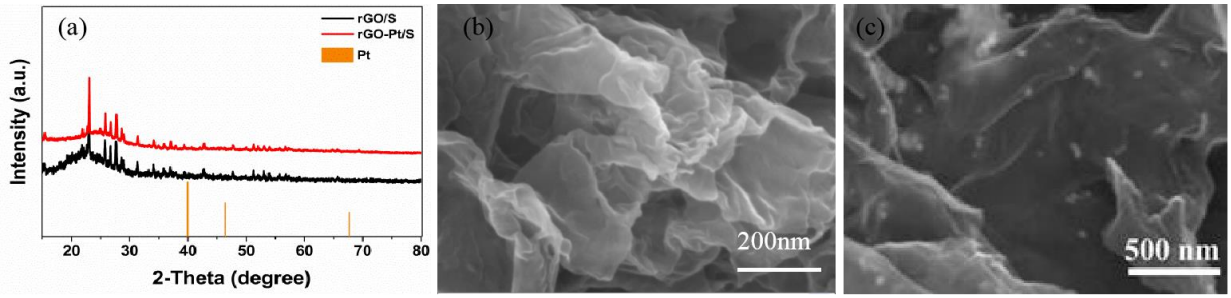

Figure 1. (a) XRD patterns of rGO/S and rGO-Pt/S. (b) (c) SEM images of rGO and rGO-Pt.

To our surprise, it can still observe that the luminous Pt nanoparticles were dotted on the rGO-Pt/S composite after the encapsulation of sulfur, as displayed by the SEM image in Figure 1c. In view of this fact, X-ray photoelectron spectroscopy (XPS) measurements further investigated and understood the properties of rGO-Pt/S composite. Figure 2a presents Pt 4f doublet with binding energy of Pt $4f_{7/2}$ and Pt $4f_{5/2}$ peaks at 71.8 eV and 74.9 eV,[48] confirming the formation of metallic Pt from Pt ions. The deconvolution of the S2p region spectrum yielded four individual component peaks (Figure 2b), corresponding to the S-S bond (163.6 eV and 164.8 eV) and S-O species (164.3 eV and 165.3 eV), respectively.[49, 50] In addition, a weak broad peak at 168.6 eV is likely attributed to the sulfate species due to the surface oxidation of sulfur. Other than that, no other characteristic peaks could be further fitted. It is obvious that polar metal Pt play no role in controlling the distribution of sulfur. Meanwhile, the divided high-resolution C1s spectra in Figure 2c can be identified as C-C bond (284.1 eV), C=N bond (284.5 eV), C-O bond (285.6 eV), and C=O bond (288.3 eV), respectively.[51] These imply oxygen doping on the graphene skeleton. The existence of oxygen-containing functional groups is favorable for

anchoring sulfur and inhibiting the diffusion of PS. The rGO/S sample shows similar XPS spectrum to that of rGO-Pt/S.

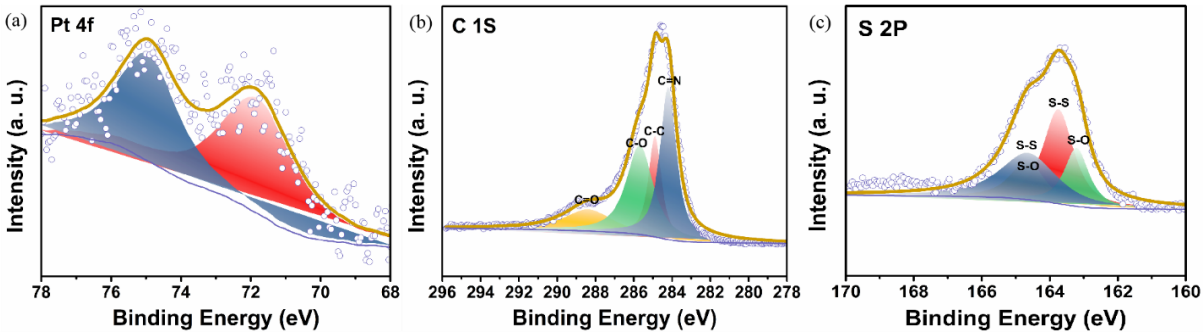

Figure 2. (a) High-resolution Pt 4f, C 1s, and S 2p spectra of rGO-Pt/S.

Transmission electron microscope (TEM) was also used to examine microstructure and morphology of rGO/S and rGO-Pt/S composite. Owing to high-energy electron beam is easily susceptible to the instantaneous sublimation of sulfur.[52-54] Thereby, only transparent and thin rGO sheets with wrinkled and folded regions could be seen but the crystalline structure of sulfur could not be determined in Figure 3a. Interestingly, it is hard to differentiate characteristic peaks of Pt in the XRD pattern (Figure 1a). However, Figure 3b clearly shows the Pt nanoparticles with size of 3-5 nm are optionally adhered to the surface of rGO. Compared to high sulfur content in rGO-Pt/S electrode, the small number of Pt nanoparticles easily overlap with sulfur at the peak position lead to relatively weak detection intensity. What is more, energy dispersive X-ray spectroscopic (EDX) analysis proves that Pt nanoparticles are homogeneously distributed throughout the carbon framework and sulfur is evenly implanted within rGO-Pt/S composite (Figure 3c).

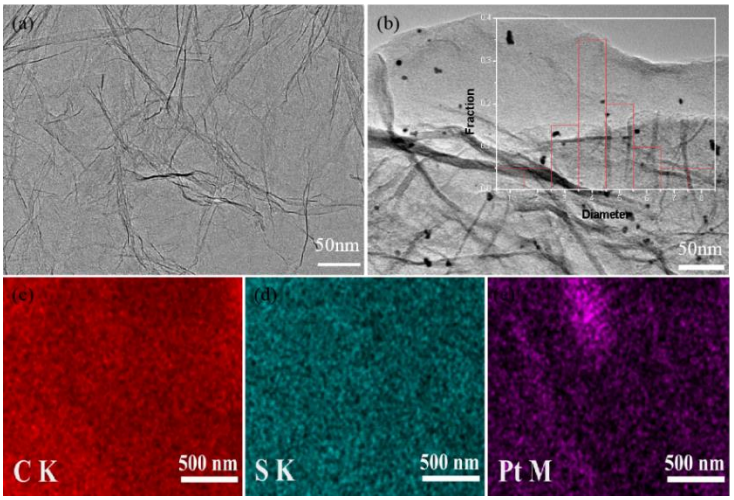

Figure 3. TEM images and the corresponding elemental mapping of (a) rGO and (b, c, d, e) rGO-Pt (the histogram inserted is the size distribution of Pt nanoparticles).

To demonstrate the positive effect of Pt on the performance of Li-S batteries, coin-type half-cells were fabricated using the aforementioned composites as the cathodes. Cyclic voltammetry (CV) was first measured at a slow scan rate of 0.05 mV s^{-1} between 1.5 V and 2.8 V. The rGO/S and rGO-Pt/S electrode show similar electrochemical characteristics, as displayed in Figure 4a, b.

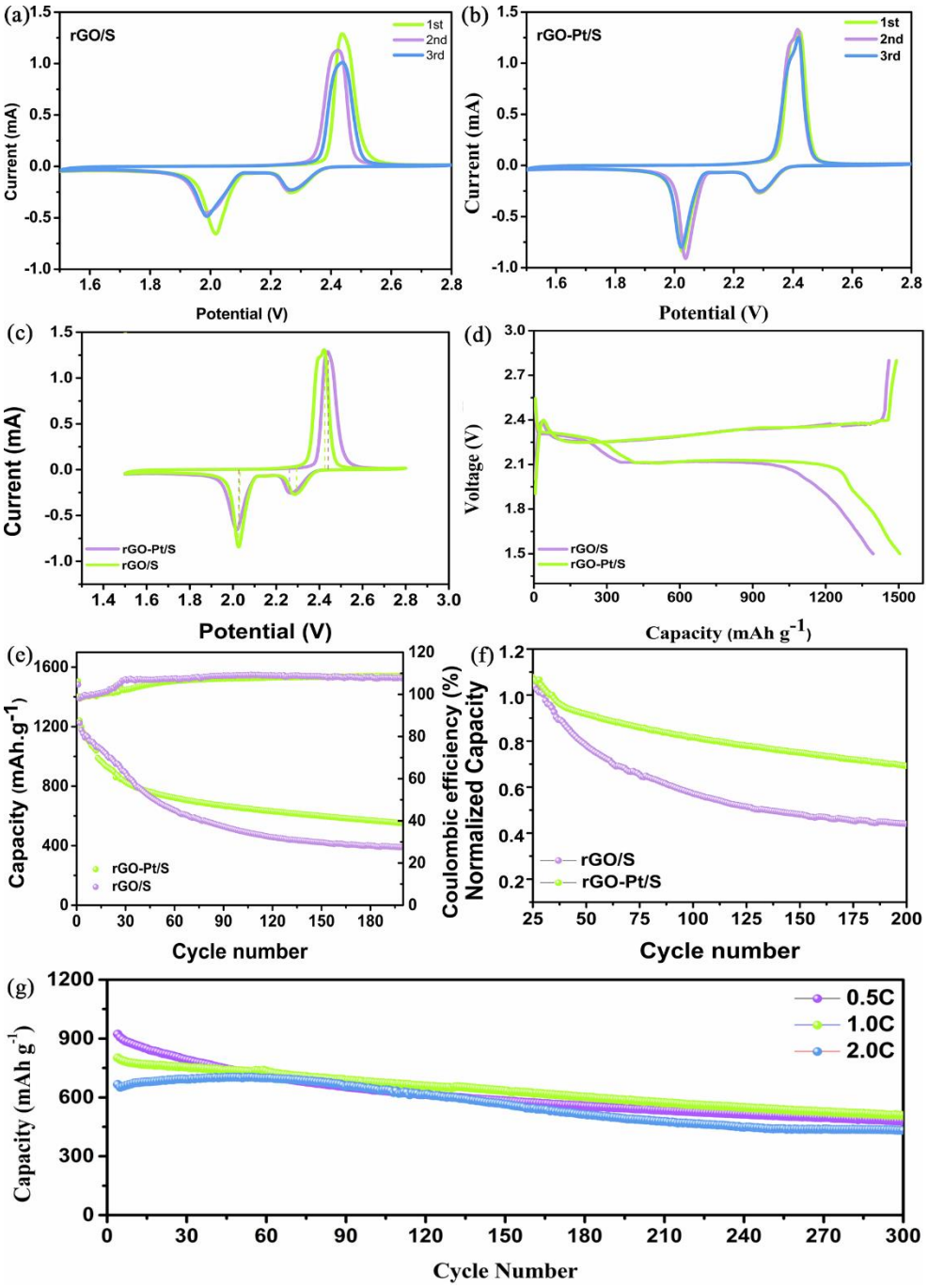

Figure 4. Comparison of electrochemical properties of both electrodes. The CV curves of (a) rGO/S, (b) rGO-Pt/S electrode, and (c) both electrodes in the first cycle. (d) Cycling performance of rGO/S and rGO-Pt/S electrode at 0.2 C rate within a potential window of 1.5−2.8 V *vs*. Li^+/Li. (e) The first discharge/charge voltage profiles of rGO/S and rGO-Pt/S electrode. (f) normalized discharge capacity against cycle number (g) Long-term performance of rGO-Pt/S electrode at 0.5 C, 1C and 2C rate.

Under cathodic current, the CV plots exhibited two reductive peaks at ~2.3 V and ~2.1 V, corresponding to the transformation of solid sulfur to soluble Li_2S_x ($4 < x < 8$) and further reduction to Li_2S_2/Li_2S.[55] On forward scan, an oxidation peak at ~2.4 V was observed attributing to the conversion of short-chain PS to solid sulfur.[56] On careful observation, two distinguishable oxidation peaks exist and overlap with each other that implied the better reversibility of reaction for rGO-Pt/S electrode. In addition, the first cycle peak potential along with potentiostatic polarization were quantified and summarized in Figure 4c. The decreased peak separation indicated the lower polarization of rGO-Pt/S electrode than that of rGO/S electrode (Table S1). It is well known that the metallic Pt catalyst is used to enhance the electrochemical hydrogen insertion into porous carbon materials because of the spillover effect on Pt.[57] Similarly, active sulfur deposited near the metallic Pt can preferentially obtain electrons from the surface of the Pt nanoparticles to reduce potential hysteresis. What is more, little difference in peak positions was observed at subsequent cycles, suggesting good stability of rGO-Pt/S electrode. However, the results for rGO/S electrode was less-than-brilliant. The positive shift in reduction peak and negative shift in oxidation peak along with sharply deforming and widening, reflecting the gradual increased polarization and sluggish reaction kinetics. Noticeably, as similar with the previous reports, [58,59] there is no observable evidence showing that all materials based on graphene have the problem of redox peak position shifted. It shows that Pt NPs loaded can enhance the electrochemical kinetics and decrease the cell polarization. All of the aforementioned results demonstrate superior catalytic properties toward the PS conversion process provided by the Pt nanoparticles.

Galvanostatic measurements were further carried out to elucidate the benefits of Pt nanoparticles in the electrode. Figure 4d compares the first charge-discharge curves of rGO/S and rGO-Pt/S electrode at current density of 0.2 C (1C= 1675 mA g^{-1}) in the voltage window of sulfur electrode (1.5-2.8V*vs* Li/Li^+). Both discharge profiles show two typical plateaus at ~2.3 V and ~2.1 V consistent with CV results. The initial discharge capacity of rGO-Pt/S electrode was 1504.7 mAh g^{-1}, while rGO/S electrode delivered a discharge capacity of 1395 mAh g^{-1}, which is 7.3% higher than that of rGO/S electrode. As we known, the second discharge plateau includes a series of complicated disproportionations and plays a decisive role in discharge capacity. When the length of the second platform of rGO-Pt/S is compared to that of rGO/S, the distinguishable extension reveal Pt nanoparticles effectively absorb long-chain polysulfides and prevent them from diffusing to lithium anode and dead corners so that more polysulfides could be converted to Li_2S. Thus, rGO-Pt/S electrode exhibited higher utilization of active sulfur closer to the theoretical capacity. However, the charge capacity of rGO/S electrode was comparable to that of rGO-Pt/S electrode, which proved that Pt nanoparticles were advantageous for restricting the shuttle effect and prevent the loss of active materials. The variation of capacity and efficiency for rGO-Pt/S electrode as a function of cycle number were plotted in Figure 4e, while those of the rGO/S electrode at the same current density was also presented for comparison. The cycle stability of rGO-Pt/S electrode was superior to that of rGO/S electrode. Nevertheless, rGO-Pt/S electrode displayed slightly faster decay at the first 25 cycles compare to rGO/S electrode. In the initial cycles, sulfur content and areal sulfur loading decline with abundant dissolution and escape of PS from the rGO/S electrode, which in turn reduces the restraint for the electron and ion transfer. However, after 25 cycles, the capacity decrease continuously because of vast loss of active sulfur. The discharge capacity at 25^{th} cycle stabilized at 875.6 and 951.7 mAh g^{-1}, respectively. In the following 175 cycles, capacity gradually decreased to 551.5

mAh g^{-1} with a high capacity retention of 62.9% and a low decay rate of 0.21% per cycle for rGO-Pt/S electrode, which were much superior than those of 389 mAh g^{-1}, 40.8%, and 0.34% for rGO/S electrode. To better compared the cycling performance of Pt-doping and bare rGO/S electrode, the discharge capacity was normalized to that at the 25th cycles (Figure 4f). The cyclic stability of the two materials showed a strong contrast. Especially between the 25th and 125th cycles, the rGO/S electrode exhibited a high capacity decay of 48% per 100 cycles, while the rGO-Pt/S electrode counterpart decayed as little as 25% per 100 cycles. Obviously, Pt nanoparticles here act a pivotal part in the outstanding capacity and cycle stability of rGO-Pt/S electrode. All of the aforementioned results can be ascribed to three possible reasons. First, the electron transfer path is effectively shortened, which enhance reaction kinetics. Second, a higher affinity between Pt nanoparticles and PS is conducive to anchoring and controlling nucleation of PS. Third, Pt nanoparticles catalyze conversion of Li_2S_2/Li_2S back to long-chain PS and elemental sulfur in the subsequent redox process. This has also been further verified from the Coulomb efficiency.

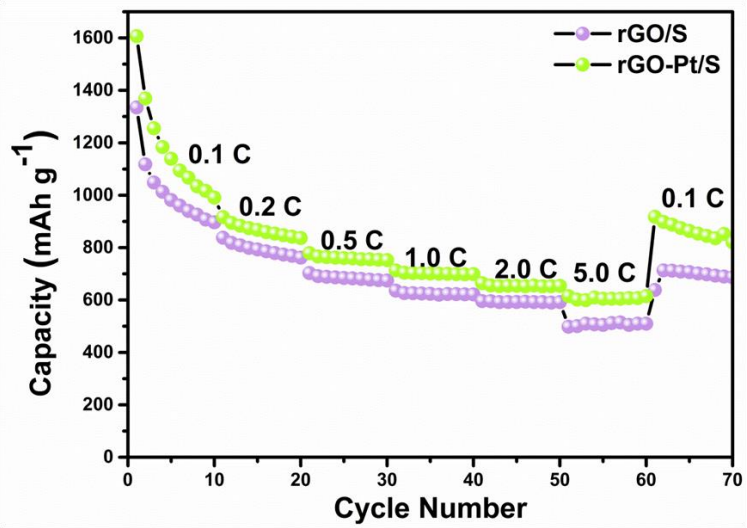

Figure 5. The rate performance of electrodes at the rate varied from 0.1 to 5 C.

Additionally, rGO-Pt/S electrode was carried out at high current after an initial three-cycle activation at a low current density of 0.05 C to examine the potential for high-power storage. As shown in Figure 4g, it carried the initial capactiy of 912.6, 796.9, and 664.8 mAh g^{-1} at rates of 0.5, 1, and 2 C, respectively and still delivered a high reversible capacity of 513.2, 533.0, and 453.0 mAh g^{-1} with a lifetime of more than 300 cycles, corresponding to a capacity diminishment of 0.14%, 0.11% and 0.10%, respectively. Electrochemical performances of rGO/S and rGO-Pt/S at different rates were depicted in Figure 5. It is apparent that rGO-Pt/S achieved the best rate behavior. The discharge capacities of 1606.9, 916.5, 778.9, 713.0, and 664.5 mAh g^{-1} were well-achieved at 0.1, 0.2, 0.5, 1, and 2 C for rGO-Pt/S electrode. Even when the current density was up to 5 C, such a high capacity of 614.9 mAh g^{-1} could still be obtained. Moreover, when the current density is returned to 0.1 C, the reversible capacity recovered to 761.5 mAh g^{-1}, indicating the good electrode stability. The rGO/S electrode, on the

contrary, exhibited discharge capacities of 1334.9, 837.6, 703.3, 635.8, 596.3, and 498.1 mAh g^{-1} at 0.1, 0.2, 0.5, 1, 2, and 5C. However, the capacity cannot restore to the primary level when the current density was recovered to 0.1 C. These results demonstrated that Pt can not only improve conductivity of electrode, but also accelerate reaction kinetics. Recently, researchers bring electrocatalysis principles to the Li-S battery configuration to stabilize the PS shuttle process and to enhance the rate capabilities. Pt/graphene have exhibited reduced overpotential and excellent specific capacity over pristine graphene electrodes. [60,61] Therefore, Pt-based nanocrystals with outer Pt-rich layers is a feasible way to obtain a novel material with catalytic properties to lithium sulfur battery. Additionally, Pt as an electrocatalyst can help to convert polysulfide deposits back to soluble long-chain polysulfide and hence enhance reaction kinetics and retain high Coulombic efficiency. Many related research have explored this issue in depth. [62]

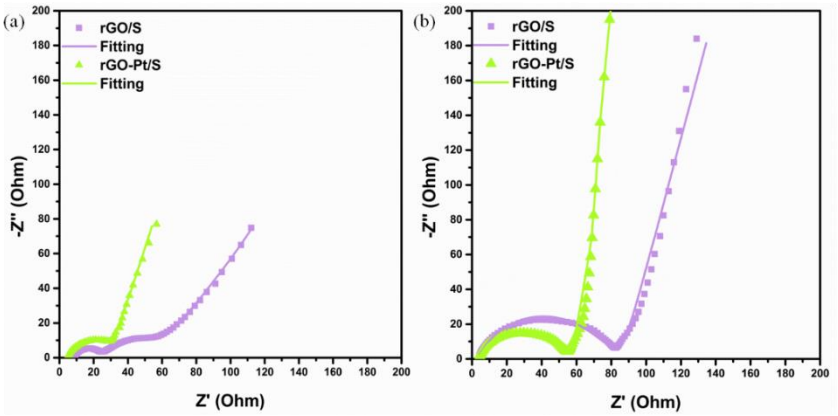

Figure 6. (a) Nyquist plots of EIS spectra for rGO/S and rGO-Pt/S electrodes at different cycles: (a) fresh cell and (b) after 200 cycles.

Further, electrochemical impedance spectra (EIS) were conducted to excavated the electrocatalytic influence on charge-transfer resistance. The Nyquist plots for fresh cells were displayed in Figure 6a. Both proflies were composed of a depressed semicircle in the high-medium frequency region accompany with a sloping line in the low frequency region, corresponding to the charge transfer resistance (R_{ct}) and diffusion-controlled Warburg impedance.[63] From the fitting results listed in Table S2, the R_{ct} of rGO-Pt/S electrode (46.77 Ω) was lower than that of rGO/S electrode (71.64 Ω), indicating the excellent electron and ion transfer kinetics associated with Pt-doping. However, in marked contrast to rGO-Pt/S electrode, the EIS of rGO/S electrode embodied an extra semicircle in the high-medium frequency region after 200 cycles, which can be attributed to the deposition of unreduced insoluble products on electrode surface. Moreover, the R_{ct} of rGO-Pt/S electrode significantly decreased after the long cycling suggesting Pt trend to migrated active materials to the electrochemically favorable position. Interestingly, rGO/S electrode also exhibited lower charge transfer resistance. In the absence of Pt, the dissolution of PS lead to reducing the abundance of active sulfur on the surface of graphene, which in turn shorten electron/ ion transfer path. All results are direct evidence for electrocatalysis of Pt towards conversion of PS.

4. CONCLUSION

Here, we introduce an electrocatalysis concept in Li/S battery configuration. The Pt nanoparticles with size of 3-5 nm are well scattered on the surface of rGO. In presence of electrocatalyst Pt, the rGO-Pt/S electrode has obtained a reversible capacity of 551.5 mAh g^{-1} with a high capacity retention of 62.9% and a low decay rate of 0.21% per cycle at 0.2 C, which is 29.5% enhancement in capacity over that of Pt-free rGO/S electrode. In addition, it also enabled a sustainable cyclic performance over 300 cycles at a high current density of 2 C accompanied by a capacity decay rate as small as 0.1% per cycle. Furthermore, excellent rate capability was also realized with a capacity of 614.9 mAh g^{-1} at 5 C. Compared to many previous reports, the rGO-Pt/S have improved mass transfer, poison resistance and stable loading of smaller Pt particles as well as their inherent electrical conductivity and chemical inertia, therefore, the rGO-Pt/S shows much higher activity and stability than before.[64,65] All of the enhancement can be attribute to three aspects: (1) Pt nanoparticles improve the conductivity of electrode; (2) Pt nanoparticles serve as the anchors to effectively immobilize soluble PS and mitigate shuttle effect to retarded the loss of active materials; (3) Pt nanoparticles accelerate reaction kinetics and catalyze the conversion of Li_2S_2/Li_2S to long-chain PS and sulfur without allowing them to precipitate much on the electrode in the subsequent charging process. We believe the electrocatalytic concept in emerging Li/S chemistries will open a new avenue for developing efficient energy storage technologies.

ACKNOWLEDGEMENT
This work was partially supported by the National Natural Science Foundation of China (5167614, 11474226), Fundamental Research Funds for the Central Universities (WUT: 2018-IB-028; 2018-IB-022; 2019-IB-004).

References

1. L. Fan, M. Li, X. Li, W. Xiao, Z. Chen, J. Lu, *Energy Storage Mater*., 8 (2019) 363.
2. J. He, A. Manthiram, *Energy Storage Mater*., 9 (2019) 3.
3. S. Li, B. Jin, X. Zhai, H. Li and Q. Jiang, *Chem Select*, 3 (2018) 2249.
4. J. Liu, M. Wang, N. Xu, T. Qian and C. Yan, *Energy Storage Mater*., 15 (2018) 59.
5. H. Yang, C. Guo, J. Chen, A. Naveed, J. Yang, Y. Nuli and J. Wang, *Angew. Chem. Int. Edit.*, 58 (2019) 793.
6. J. Zhu, P. Zhu, C. Yan, X. Dong and X. Zhang, *Pro. Polym. Sci*., 90 (2019) 125.
7. A. Manthiram, S.H. Chung and C. Zu, *Adv Mater*., 27 (2015) 1999.
8. D. Liu, Y. Li, D. Zheng, G. Wang, D. Qu, Z.Z. Xie, C. Li, J. Lei and D. Qu, *Chem Select*, 2 (2017) 7164.
9. R. Fang, S. Zhao, Z. Sun, W. Wang, H.M. Cheng and F. Li, *Adv Mater*., 29 (2017) 1606823.
10. D. Qu, R Li, X.X. Zhu, K. Chen , Y.F. Shen, D Liu, Z.Y.Ma, S.C. Zhang , Z.Z. Xie, J.S Li, J.H. Lei and H.L. Tang, *Int. J. Electrochem. Sci*., 13(2018) 11298.
11. Z.Yan, Q. Guo, Z. Jiang, W. Wei, L. Gao and J. Xie, *J. Power Sources*, 284 (2015) 500.
12. G.Yi, Z. Chang, G. Liu and G. Yang, *Int. J. Electrochem. Sci.*, 14 (2019) 7238.
13. J.Wang, Y.C. Lan, L. Yan, Y.F. Li and Z.Q. Shi, *Int. J. Electrochem. Sci.*, 13 (2018) 7670.
14. S.H. Chung and A. Manthiram, *Adv Mater*., 26 (2014) 7353.
15. X. Ji, K.T. Lee and L.F. Nazar, *Nat. Mater*., 8 (2009) 502.

16. W. Yang, W. Yang, A. Song, G. Sun and G. Shao, *Nanoscale*, 10 (2018) 820.
17. M. Yan, H. Chen, Y. Yu, H. Zhao, C.F. Li, Z.Y. Hu, P. Wu, L. Chen, H. Wang, D. Peng, H. Gao, T. Hasan, Y. Li and B.L. Su, *Adv. Energy Mater*., 8 (2018) 1801066.
18. Y. Yuan, G. Tan, J. Wen, J. Lu, L. Ma, C. Liu, X. Zuo, R.S. Yassar, T. Wu and K. Amine, *Adv. Funct. Mater.*, 28 (2018) 1706443.
19. K. Shen, H. Mei, B. Li, J. Ding and S. Yang, *Adv. Energy Mater*., 8 (2018) 1701527.
20. A.Q. Xia, C.J. Xing, W.Y. Qiao and Z. Zhao, *Chemistry & Bioengineering,* 6 (2018)7.
21. W. Wang, X.C. Xia, Y.C. Jiang and Z.J. Hong, *Chemistry & Bioengineering*, 6 (2018) 50..
22. H. Zhang, L. Zhou, X. Huang, H. Song and C. Yu, *Nano Res*., 8 (2016) 3730.
23. F. Wu, J. Li, Y. Su, J. Wang, W. Yang, N. Li, L. Chen, S. Chen, R. Chen and L. Bao, *Nano Lett*., 23 (2016) 5490.
24. Z. Cheng, Z. Xiao, H. Pan, S. Wang and R. Wang, *Adv. Energy Mater.*, 9 (2017) 1702337.
25. M. Fang, Z. Chen, Y. Liu, J. Quan, C. Yang, L. Zhu, Q. Xu and Q. Xu, *J. Mater. Chem. A*., 6 (2018) 1633.
26. F. Pei, L. Lin, D. Ou, Z. Zheng, S. Mo, X. Fang and N. Zheng, *Nat Commun.*, 8 (2017) 482.
27. S.K. Park, J.K. Lee and Y.C. Kang, *Adv. Funct. Mater*., 28 (2018) 1705264.
28. L. Ni, Z. Wu, G. Zhao, C. Sun, C. Zhou, X. Gong and G. Diao, *Small*, 13 (2017) 1603466.
29. X. Wu, X. Yuan, J. Yu, J. Liu, F. Wang, L. Fu, W. Zhou, Y. Zhu, Q. Zhou and Y. Wu, *Nanoscale*, 9 (2017) 11007.
30. D.R. Deng, F. Xue, Y.J. Jia, J.C. Ye, C.D. Bai, M.S. Zheng, Q.F. Dong, *ACS Nano*, 11 (2017) 6031.
31. T. Takeuchi, H. Sakaebe, H. Kageyama, H. Senoh, T. Sakai and K. Tatsumi, J. Power Sources., 195 (2010) 2928-2934.
32. W. Zhang, P. Liu, J. Pan, X.Yang, J. Liu, H. Xu and Z. Ouyang, *Int. J. Electrochem. Sci.* 12 (2017) 11116.
33. A. Hofmann, D. Fronczek and W. Bessler, *J. Power Sources*, 259 (2014) 305.
34. T. Takeuchi, H. Sakaebe, H. Kageyama, H. Senoh, T. Sakai and K. Tatsumi, *J. Power Sources*, 195 (2010) 2930.
35. S.S. Zhang, *J. Power Sources*, 231 (2013) 157.
36. D. Qu, X. Zhu, D. Zheng, Y. Zheng, D. Liu, Z. Xie, H. Tang, J. Wen, X. You, L. Xiao, J. Lei and D. Qu, *Electrochem. Acta*., 174 (2015) 403.
37. B. Liu, W. Wang, H. Li, Z. Jian, Y. Xing and S. Zhang, *Int. J. Electrochem. Sci.*, 13 (2018) 6875.
38. I.E. L. Stephens, A.Z. Caterina Ducati and D.J. Fray, *J. Electrochem. Soc.*, 160 (2013) A759.
39. F. Hao, P. Dong, J. Zhang, Y. Zhang, P.E. Loya, R.H. Hauge, J. Li, J. Lou and H. Lin, *Sci. Rep*., 2 (2012) 368.
40. C.C. You, J.R. Yang, N. Tian and L. Ma, *Int. J. Electrochem. Sci.*, 14 (2019) 8600.
41. J. Cai, C. Wu, Y. Zhu, K. Zhang and P. K. Shen, *J. Power Sources*, 341 (2017) 165.
42. N. Thangavel, D. Gopalakrishnan and L. Arava, *J. Phys. Chem C*., 121 (2017) 12722.
43. E. Randviir and C. Banks, *Electroanal.,* 26 (2014) 79.
44. Z. Schaefer, M. Gross, M. Hickner and R. Schaak, *Angew. Chem. Int. Edit.,* 49 (2010) 7047.
45. H. Huang and X. Wang, *J. Mater. Chem. A.,* 2 (2014) 6279.
46. W. Yuan, S. Lu, Y. Xiang and S.P. Jiang, *RSC Adv.*, 4 (2014) 46275.
47. M. Chen, Q. Lu, S. Jiang, C. Huang, X. Wang, B. Wu, K. Xiang and Y. Wu, *Chem. Eng. J.,* 335 (2018) 831.
48. C. Jin, W. Zhang, Z. Zhuang, J. Wang, H. Huang, Y. Gan, Y. Xia, C. Liang, J. Zhang and X. Tao, *J. Mater. Chem. A.,* 5 (2017) 632.
49. Z. Lin, L. Xia, W. Huang, Z. Xi, W. Yun and Z. Shan, *Chem. electro. chem*., 4 (2017) 10.
50. L. Yang, K.Wei, X. Li, C. Huang, R. Shui and G. He, *Small*, 34 (2019) 15.
51. Q. Shu, *Mater. Res. Express*, 6 (2019) 055508.
52. Z. Lin, X. Li and W. Huang, *Chem. Electro. Chem*., 4 (2017) 2580.
53. D. Marcano, D. Kosynkin, J. Berlin, A. Sinitskii, Z.Sun, A. Slesarev, L. Alemany, W. Lu and J. Tour,

ACS Nano., 4 (2010) 4809.
54. M. Yu, J. Ma, M. Xie, H. Song, F. Tian, S. Xu, Y. Zhou, B. Li, D. Wu, H. Qiu and R. Wang, *Adv. Energy Mater.*, 7 (2017) 1602347.
55. H. Al Salem, G. Babu, C.V. Rao and L.M. Arava, *J. Am. Chem Soc.*, 137 (2015) 11542.
56. C. Fan, P. Xiao, H. Li, H. Wang, L. Zhang, H. Sun, X. Wu, H. Xie and J. Zhang, *ACS Appl. Mater. Interfaces*, 7 (2015) 27963.
57. Y. Zhong, S. Wang, Y. Sha, M. Liu, R. Cai, L. Li and Z. Shao, *J. Mater. Chem. A.,* 90 (2016) 9530.
58. F. Gao, X. Yan, Z. Wei, M. Qu and W. Fan, *Int. J. Electrochem. Sci*., 14 (2019) 3308.
59. J.R. Xiao, Z.Y. Yang, H.Z. Wang, Y.F. Guo and Z.R. Tao, *Int. J. Electrochem. Sci*., 12 (2017) 11113.
60. P. Andrea, D. Hendrix, C. Pascale, G. Catherine, G. Gabriel, D. Nicolas, Z. Wen, V. Ashok, G. Abdelbast and Z. Karim, *J. Power Sources*, 427 (2019) 204.
61. Z.Q. Li, J. Xu, J. WANG, D.F. iu, S.Z. Hu and X.S. Zhang, *Int. J. Electrochem. Sci*., 4 (2019) 635.
62. Z. Ma, L. Tao, D. Liu, Z. Li, Y. Zhang, Z. Liu, H. Liu, R. Chen, J. Huo and S. Wang, *J. Materials Chem. A*., 5 (2017) 9415.
63. X. Ye, J. Ma, Y.S. Hu, H. Wei, and F. Ye, *J. Mater. Chem. A.*, 4 (2016) 777.
64. C. Wu, J. Maier and Y. Yu, *Adv. Mater.*, 28 (2016) 178.
65. Q. Li, Z. Zhang, K. Zhang, J. Fang, Y. Lai and J. Li, *J. Power Sources*, 256 (2014) 140.